Vogel–Fulcher analysis of relaxor dielectrics with the tetragonal tungsten bronze structure: $Ba_6MNb_9O_{30}$ (M = Ga, Sc, In)

Andrei Rotaru · Finlay D. Morrison

Abstract In-depth analysis of the relaxor behaviour of $Ba_6MNb_9O_{30}$ (M = Ga, Sc, In) tetragonal tungsten bronze (TTB) ceramics was carried out. Powder X-ray diffraction and scanning electron microscopy were performed in order to confirm the formation of desired phases and to determine the microstructure. Low-temperature dielectric spectroscopy was used in order to characterise the dielectric properties of these materials; the degree of relaxor behaviour was investigated in relation with the increase of ionic radius of the M cation on the B-site of the TTB structure. The dynamics of dielectric relaxation of dipoles was studied by fitting the dielectric permittivity data to the Vogel–Fulcher (VF) model in order to monitor the reproducibility and validity of the physical results. Restrictions to the VF fit were attempted besides the regular "free-fit" by constraining some of the fundamental relaxation parameters to physically sensible values. We show that VF fits are very sensitive to the fitting range resulting in a large range of fundamental parameters for the dielectric relaxation processes, and that the restriction of the frequency domain due to experimental noise or instrumentation limits has a dramatic influence on the values obtained.

Keywords Canonical relaxors · Low-temperature dielectric spectroscopy · Dipolar relaxation · Electroceramics · Tetragonal tungsten bronzes · Vogel–Fulcher model

A. Rotaru · F. D. Morrison (✉)
EaStCHEM Research School of Chemistry, University of St Andrews, North Haugh, St Andrews, Fife KY16 9ST, Scotland, UK
e-mail: finlay.morrison@st-andrews.ac.uk

A. Rotaru
Laser Department, National Institute for Laser, Plasma and Radiation Physics (INFLPR), Bvd. Atomistilor, Nr. 409, Măgurele (Ilfov), 077125 Bucharest, Romania

A. Rotaru
Faculty of Mathematics and Natural Sciences, University of Craiova, A.I. Cuza Str, Nr. 13, Craiova, Romania

Introduction

Polar dielectrics, particularly ferroelectrics, are used in a wide range of electronic devices including: capacitors, electro-optic switches, non-volatile memory chips and a number of piezoelectric transducers and sensors. The materials in use today are often Pb containing, e.g. $Pb(Zr,Ti)O_3$ (PZT) [1], or have limited operating temperatures (e.g. $BaTiO_3$, T_C = 130 °C) [2], and therefore new materials are required for future development. The recent renaissance in the search for novel dielectrics and mainly for multiferroics materials (possessing in the same chemical compound at least two of the following ferroic behaviour: ferroelectric, ferromagnetic/ antiferromagnetic or ferroelastic, while by imposing a certain external field one may control a different property) and magnetoelectrics (i.e. coupling of the dielectric and magnetic response) [3, 4] has largely focussed on materials with the perovskite structure [5]. The single-phase perovskite-based multiferroic materials ($BiFeO_3$, $BiMnO_3$, $HoMnO_3$ and $TbMnO_3$) [6–10] have simpler structures by comparison, and their properties are better understood [11]. However, the perovskite structure may evolve to other perovskite-related structures in different ways (all imposed by the N_A/N_B ratio of the A- and B-sites), which have even greater compositional flexibility and may offer better properties over larger

operating ranges. Therefore, it is worth directing more attention to these "superstructures" such as: double perovskites with the unit cell edges of a perovskite doubled as a result of cation ordering on the B-site ($A_2BB'O_6$); the Ruddlesden–Popper structures which have perovskite blocks intercalated by (AO) units ($A_{n+1}B_nO_{3n+1}$); and especially the tetragonal tungsten bronze (TTB) structure (($A1)_2(A2)_4(C)_4(B1)_2(B2)_8O_{30}$), where the inclusion of particular metals into the five different TTB sites [12] raises the possibility of fine tuning both the electric and magnetic behaviour [11].

As its nominal formula and related structure (Fig. 1) indicate, the possibilities to accommodate various cations within the five sites of the very flexible tetragonal tungsten bronze (TTB) structure give the prospect of finding many interesting and useful novel materials by tuning the electric and magnetic properties through compositional variation [12, 13]. The TTB structure begins with a repetitive perovskite unit in the middle, but the additional corner-sharing BO_6 octahedra, bringing the total B-sites to ten per unit cell, create three types of channels in the structure: two different A-sites and one C-site. There are two A1 sites (12-coordinated) defined by 8 octahedra, four larger A2 sites (15-coordinated) defined by 10 octahedra and four trigonal C-sites (9-coordinated) defined by 6 octahedra. In addition, the BO_6 octahedra are non-equivalent (two B1 sites and eight B2 sites). Usually, the A-sites are occupied by large cations such as those belonging to the *s*-block (i.e. K^+, Na^+, Ba^{2+}, Sr^{2+}, Ca^{2+}) or lanthanides from the *f*-block (i.e. La^{3+}, Ce^{3+}, Nd^{3+}, etc.) [14–16], while the B-sites at the centre of the oxygen octahedral are filled with smaller *d*-block cations (i.e. Nb^{5+}, W^{6+}, Cr^{3+}, Mn^{3+}, Fe^{3+}, Ti^{4+}, etc.) [17, 18]. The C-sites may be occupied by small cations (i.e. Li^+), but this is not always required. The presence of non-equivalent A- and B-sites provides an
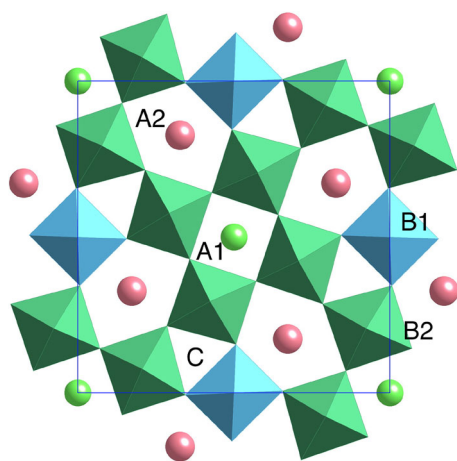
extra degree of freedom, which can be transduced into the possibility to confine magnetic and ferroelectric ordering to separate sublattices. This rich diversity of elements which can be incorporated into the TTB structure allows for compositional tuning that has been exploited for the development of new phases ranging from ferroelectrics [13, 19, 20] to microwave dielectrics [21, 22] and to ionic conductors [23].

Given the interest for finding ferroelectric ferrimagnets in the 1960s and 1970s, it is no surprise that the search included some TTB oxides. Although several studies attempted to incorporate cations with uncompensated spins into the structure for inducing magnetic ordering, the findings were contradictory and in some cases even incomplete. Whilst ferroelectric TTBs (including $Ba_2NaNb_5O_{15}$ [24–26] and $(Ba,Sr)Nb_2O_6$ [27–29]) were widely investigated during those years, the amount of study is surprisingly limited relatively to perovskites and our understanding of manipulating this structure type is still poor. In the latest years, there has been a resurgence in research dedicated to the discovery of novel TTB ferroelectric and ferroelectric-related (i.e. relaxors) materials, with a focus on the $Ba_6FeNb_9O_{30}$ (BFNO) compound and some related solid solutions with lanthanides [30–34]. Regarding the physical properties of BFNO, it was previously reported to be ferroelectric with T_C values either in the range 133–138 K [35] or 570–583 K [36, 37]. In all cases, these reports were based on the observation of a peak in the dielectric permittivity obtained using fixed frequency measurements. Later studies by Arnold and Morrison [12] and subsequently by Liu et al. [38], using variable frequency dielectric spectroscopy, showed that in fact this compound displays relaxor-type behaviour [39–41], with peak maxima in the dielectric permittivity occurring in the temperature range 130–150 K. Preliminary data from this study indicated that BFNO is not electrically homogeneous [32], with oxygen vacancy gradients due to the variable oxidation state of Fe (Fe^{3+}/Fe^{2+}). Both low-temperature dielectric spectroscopic data and high-temperature impedance spectroscopy measurements revealed a higher number of electroactive regions than expected. In order to avoid this additional complication during the study of this type of materials, Fe^{3+} was replaced by other trivalent species which do not have variable oxidation states [12, 42, 43].

The new family of relaxor TTBs of composition $Ba_6M^{3+}Nb_9O_{30}$, where the trivalent species do not have variable oxidation states (e.g. Ga^{3+}, Sc^{3+}, In^{3+} and Y^{3+}), was reported by Arnold & Morrison [12]; it was shown that with increasing ionic radii of the M^{3+} ions in $Ba_6M^{3+}Nb_9O_{30}$ TTBs ($M^{3+} = Ga^{3+}$, Fe^{3+}, Sc^{3+}, In^{3+} of Y^{3+}), the temperature of the permittivity peak maximum (T_m) is dramatically shifted to higher temperatures [12]. This is in contrast with previous data reported for $Ba_6M_2^{4+}Nb_8O_{30}$

Fig. 1 Representation of the tetragonal tungsten bronze (TTB) structure

materials which exhibit decreasing T_m or T_C (temperatures of the maximum dielectric permittivity) with increasing M^{4+} ionic radius [44, 45]; however, these seemingly contradictory results were explained by the polarisation/polar ordering which becomes increasingly stabilised to higher temperatures with increasing tetragonality (c/a) [12]. Irrespective of the valence of the metal ion in the TTB, the transition temperature increases with increasing tetragonality (strain) [12]. The full structural and dielectric characterisation of $Ba_6M^{3+}Nb_9O_{30}$ ($M^{3+} = Ga^{3+}$, Sc^{3+} and In^{3+}) TTB relaxor materials (relaxor dielectrics, of "dipole glass"-like type model) was presented [42], while characteristic temperature parameters (e.g. standing for the freezing temperatures of dipolar relaxation) for each compound were extracted from both dielectric and crystallographic data as a function of temperature: the Vogel–Fulcher (VF) temperature, T_{VF}; T_{UDR} corresponding to absolute flattening of the dielectric loss peak in the frequency domain; and $T_{c/a}$ corresponding to the maximum crystallographic tetragonal strain. These temperature parameters were essentially coincidental and describe the slowing of dipoles on cooling and the eventual "locking" of the B-cation displacements along the c-axis (i.e. dipole freezing) [42]. A-site doping with smaller divalent cations introduces local strain which increases the dipole stability and contribution from the B2 perovskite-like octahedra; this effect, however, is not sufficient to induce dipole ordering within the solid solution limits for stability of the TTB phase [43]. By introducing fewer, smaller lanthanide cations at the A-site and with non-stoichiometry in the form of charge-compensating A-site vacancies, it is possible to induce dipole ordering and ferroelectricity. The presence of lanthanide cations with an unfilled $4f$ shell also introduces magnetic moments and the possibility of multiferroic behaviour [43]. While these observations marked steps towards quantitatively correlating the composition–structure–property relations in TTBs so that a "global" understanding of these materials similar to those in perovskites would be utilised in the design of new functional materials, the precise origin and nature of their relaxor behaviour has to be still investigated.

In this paper, we have reinvestigated the series of $Ba_6MNb_9O_{30}$ ($M =$ Ga, Sc, In) TTBs, obtained by employing a similar procedure as in Ref. [42], but the pellets were sintered for longer times (12 h) in order to further improve the microstructure. After the structural and microstructural characterisation which confirmed the formation of the desired phases, low-temperature dielectric spectroscopy was used in order to characterise the dielectric properties of these materials; this thermo-electrical method, which is one of the most wide-spread methods, is useful in the electroceramics field [46, 47] and is also very sensitive for dielectric relaxations in polymers [48, 49] or pharmaceuticals [50, 51]. The dynamics of dielectric relaxation of dipoles was studied by means of the frequency and temperature dependence of complex dielectric permittivity, $\varepsilon^*(f, T)$, data; it was generally observed that the frequency response of the real part of dielectric permittivity in relaxors has a VF form [52, 53], as was firstly indicated by Viehland et al. [54] following the idea for the slowing down of relaxation processes found in many glasses [55]. The displacement at higher temperature of the VF curves and the degree of relaxor behaviour represented by the curvature of the $\ln f$ versus T_m plot (where f is the frequency of the applied AC electric field and T_m is the temperature of maximum dielectric permittivity at frequency f) were investigated in relation with the stepwise increase of the ionic radius of the M cation on the B-site. The VF equation was used for fitting the dielectric permittivity data in order to monitor the reproducibility and validity of the physical results. Physically sensible restrictions to the fit were also investigated besides the regular "free-fit" (fixed values for T_{VF} or for f_0), as extreme possible values.

Experimental

Compositions $Ba_6MNb_9O_{30}$ ($M =$ Ga, Sc, In) were synthesised by standard solid-state techniques. Dried $BaCO_3$, Nb_2O_5, Ga_2O_3, In_2O_3, (all Aldrich, 99 + %) and Sc_2O_3 (Stanford Materials Corporation, 99.999 %) with stoichiometric ratios were ball milled until homogenized in ethanol for 5 min at 400 rpm, using a Fritsch Pulverisette 7 system with agate mortar and balls. Powders were placed on platinum foil in alumina boats and fired in a muffle furnace (static air atmosphere) straight to 600 °C. They were heated from 600 to 1,000 °C, left to decarbonate for 1 h, and then fired for 12 h at 1,250 °C. Further, they were quenched to room temperature, reground and heated at 1,250 °C for 12 h more in alumina boats inside the same muffle furnace. Finally, a third attempt for completing the reactions was carried out for 6.5 h each, at the following temperatures: 1,300 °C (for $Ba_6GaNb_9O_{30}$) and 1,350 °C (for $Ba_6ScNb_9O_{30}$ and $Ba_6InNb_9O_{30}$), in order to avoid melting. This time, radiation shields were used at both ends of the alumina tube to maintain a more stable temperature and to avoid "over-shoot" during sintering (the conditions inside the tube were still at atmospheric pressure); alumina boats were placed in the middle of the tube furnace and contained the previously ball-milled powders. For sintering the pellets, they were placed in alumina boats inside a tube furnace (as previously described) and heated to the sintering temperature. Generally, heating and cooling rates were 10 K min^{-1}. Here, in order to improve the microstructure and for the in-depth analysis of the relaxor properties in $Ba_6MNb_9O_{30}$ (where $M =$ Ga, Sc, In), new pellets were sintered for longer times (12 h here, compared

to only 6.5 h [12, 42]) at the temperatures previously reported in Ref. [42].

Phase formation was confirmed by powder X-ray diffraction collected in transmission mode using a STOE diffractometer using Cu Kα 1 radiation (40 kV and 30 mA, $\lambda = 1.54413$ Å) over the range $20 \leq 2\theta \leq 60$ ° in steps of 0.2°, lasting for approximately 10 h. Samples were ground and placed between transparent plastic foils in steel discs. The lattice parameters were obtained by refining the X-ray diffraction data by Rietveld method [56]; refinement of X-ray diffraction data was carried out using GSAS software [57]. For electron microscopy, a JEOL JSM 5600 SEM machine with attached EDX system, providing 3.5 nm resolution and a magnification of 300,000×, was utilised.

For dielectric spectroscopy measurements, Pt electrodes were applied on the pellets after quenching using a Pt paste (Gwent Electronic Materials Ltd.) and cured at 900 °C for approximately 1 h; the action was repeated for the other side of the pellet. Dielectric measurements were performed on Agilent 4294 and HP 4192A impedance analysers in the frequency range of 5 Hz–10 MHz using an AC excitation of 500 mV and in the temperature range between 50 and 340 K with the cooling rate of 2 K min^{-1} using a closed-system helium cryocooler with DE 202 cold head (A.S. Scientific products Ltd, UK) with a Sumitomo HC-2 compressor. Before starting the measurements, the samples were heated up to 340 K and kept isothermally in order to stabilise for approximately 15 min; only afterwards, the dielectric spectroscopy data were collected during cooling.

Results and discussion

(Micro)structural and dielectric results for $Ba_6MNb_9O_{30}$ (M = Ga, Sc, In) ceramics

By scanning electron microscopy (SEM), we have observed the microstructure of the ceramic pellets. All pellets were white, with no evident colour gradient on the external surfaces or fracture surfaces. A representative micrograph describing the internal ceramic microstructure of the $Ba_6GaNb_9O_{30}$ is shown in Fig. 2. The micrograph reveals a highly dense microstructure with well-bonded grains (as shown from the intragranular nature of the fracture) and with only a few isolated pores. The high processing temperatures, which are close to the melting temperatures, indicate that all $Ba_6MNb_9O_{30}$ pellets sintered well and this is consistent with the smooth and continuous surfaces in the SEM images. Dense and well-sintered pellets for the three investigated analogues of $Ba_6MNb_9O_{30}$ were obtained when using the conditions described in Table 1. Compared with the samples described in Ref.
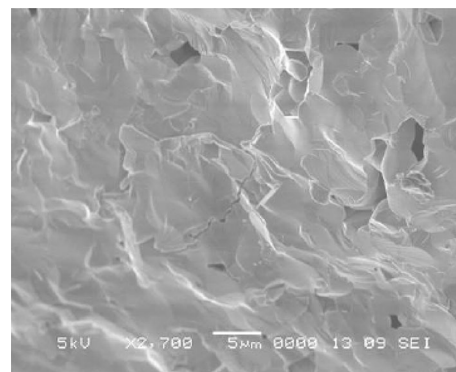

Fig. 2 SEM image of the fracture surface of a $Ba_6GaNb_9O_{30}$ pellet sintered at 1,300 °C for 12 h

Table 1 Sintering conditions and densities for $Ba_6MNb_9O_{30}$ (M = Ga, Sc, In) pellets

Compound	Sintering temp./ °C	Sintering time/h	Relative density/ %
$Ba_6GaNb_9O_{30}$	1,300	12	95.62
$Ba_6ScNb_9O_{30}$	1,350	12	92.34
$Ba_6InNb_9O_{30}$	1,350	12	95.21

[42], the relative densities improved significantly—all being above 92 % (Table 1).

Powder X-ray diffraction (PXRD) of crushed pellets was carried out to identify the compounds and to confirm that no crystallographic change had occurred during the prolonged sintering stage; the results matched those of the previously investigated initial powders described in Ref. [42]. All three data sets were refined in the space group $P4/mbm$ (No. 127) using the Rietveld method [56]—Fig. 3; the unit cell and goodness-of-fit parameters are presented in Table 2. A systematic increase in lattice parameters was observed with increasing ionic radius of the M^{3+} cation on the B-site ($r_{Ga}^{3+} = 0.62 < r_{Sc}^{3+} = 0.745 < r_{In}^{3+} = 0.80$ Å for 6-fold coordination [58]), with only a small increase in lattice parameters observed between the Sc and In analogues, but in reasonable agreement with the previous X-ray diffraction study [12]. The refinement of the X-ray diffraction data for Ga analogue includes a small amount of $Ba_5Nb_4O_{15}$ perovskite second phase, as previously discussed in Ref. [42].

Dielectric spectroscopic data in the range 50–340 K showed that all three analogue compounds exhibit characteristic relaxor behaviour, with a strong frequency dependence of the peaks in both dielectric constant and dielectric loss as a function of temperature, as observed earlier [12, 42]. Also, with increasing the average B-site ionic radii, the dielectric curves were displaced towards higher temperatures. Dielectric permittivity data for the In
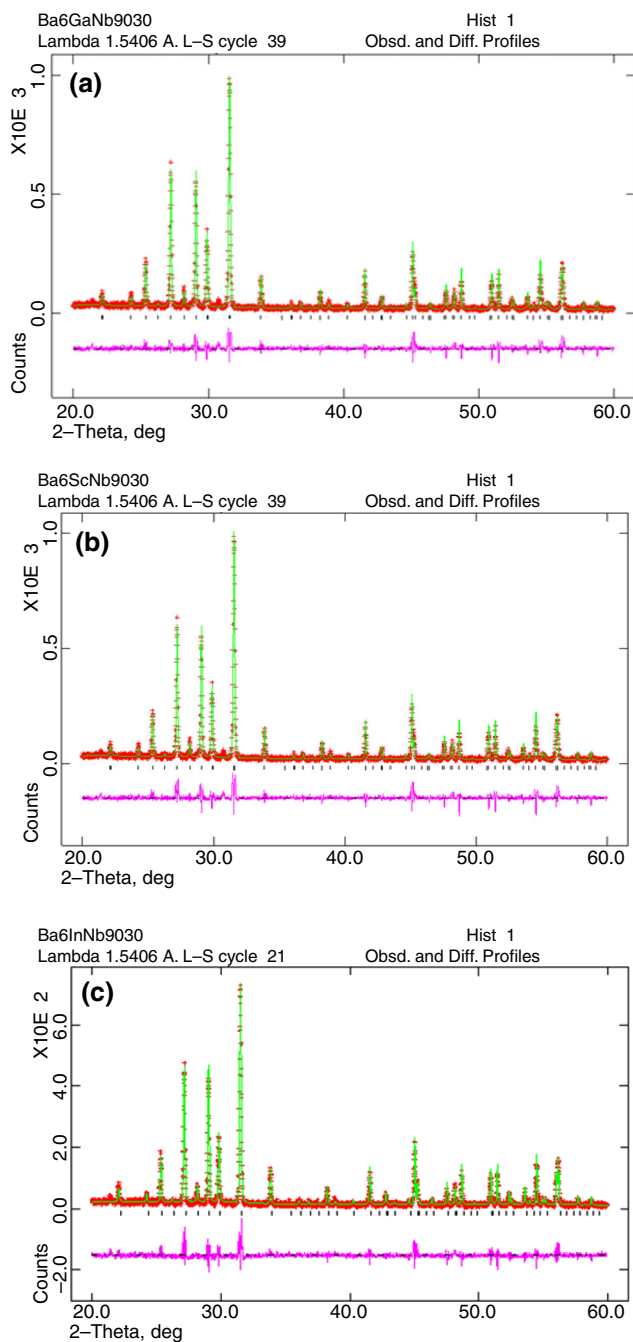
Fig. 3 Rietveld refinement profile of room-temperature PXRD data in centrosymmetric, tetragonal space group *P4/mbm* for: **a** $Ba_6GaNb_9O_{30}$; **b** $Ba_6ScNb_9O_{30}$; **c** $Ba_6InNb_9O_{30}$
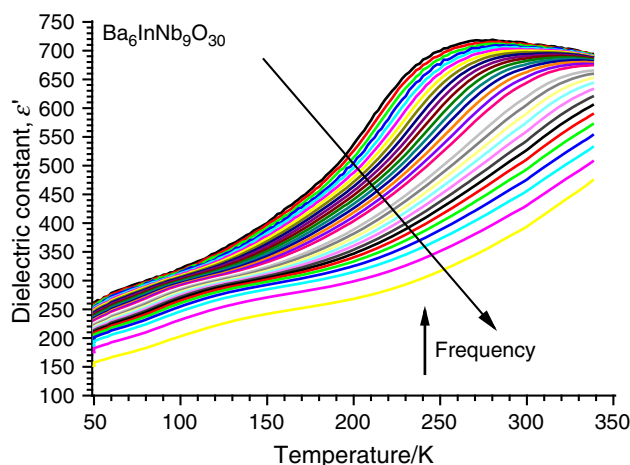

Fig. 4 Dielectric permittivity as a function of frequency and temperature for $Ba_6InNb_9O_{30}$

analogue, $Ba_6InNb_9O_{30}$, are shown in Fig. 4; for this compound, the peaks become more asymmetric and the curves flatten more at temperatures above T_m. This effect is very likely to be due to some secondary dielectric processes that overlap with the main one. Moreover, due to limitations in the experimental set-up, it is not possible to record dielectric permittivity data much above 340 K (Fig. 4), and therefore not all T_m values were able to be extracted, especially those at the highest frequencies.

While in normal ferroelectrics the dipoles spontaneously correlate, for the case of relaxors, the dipoles—although present in the material—do not coherently order in the long range (no macroscopic polarisation appears in the absence of an external electric field and no macroscopic ferroelectric transition occurs at the temperature corresponding to the maximum of the peak, T_m) [40]. The term "relaxor" is due to the dispersion in dielectric permittivity with frequency, since it takes varying times for the polarisation fluctuations to respond [59]. The relaxor behaviour within the broad group of ferroelectric ceramics is characterised by a broad maximum in the dielectric permittivity and a strong frequency dispersion within a large temperature range, below the temperature corresponding to the maximal permittivity [60]; this diffuse phase transition has been extensively studied before [61–63]. Above this temperature (in the paraelectric state), they respect the Curie–Weiss law

Table 2 Unit cell dimensions and goodness-of-fit parameters for $Ba_6M^{3+}Nb_9O_{30}$ ($M^{3+} = Ga^{3+}$, Sc^{3+}, In^{3+}) crushed pellets sintered for 12 h. XRD data refined in space group *P4/mbm*

Compound	a/Å	c/Å	V/Å^3	R/%	wR/%	χ^2
$Ba_6GaNb_9O_{30}$	12.57711(02)	3.97945(01)	629.484(04)	5.12	3.90	4.501
$Ba_6ScNb_9O_{30}$	12.66250(40)	4.01827(13)	644.285(35)	6.14	5.91	8.589
$Ba_6InNb_9O_{30}$	12.67010(40)	4.02516(15)	646.160(40)	5.34	5.96	8.201

at very high temperatures, but show significant deviations at lower temperatures due to varying degrees of localised dipole interactions. The VF model [52, 53] may describe a temperature dependence of a spectrum of relaxation times and so probes the dynamics and population profile of the dipolar response (dielectric permittivity) as a function of temperature (at $T > T_f$, where T_f represents the freezing temperature of dipolar relaxation); the modelling and analysis of the dielectric permittivity data by means of the VF model is widely used for determining the relaxation parameters that characterise the relaxation behaviour.

Vogel–Fulcher analysis of the relaxation behaviour of $Ba_6MNb_9O_{30}$ (M = Ga, Sc, In) ceramics

The aim of this work was to investigate the reproducibility and validity of the results reported previously [42, 43]. The in-depth analysis of the dielectric relaxation processes in new pellets of $Ba_6M^{3+}Nb_9O_{30}$ (M = Ga, Sc, In) with improved densities was performed by fitting the dielectric permittivity data using the VF expression (Eq. 1) [52, 53], as previously proposed by Viehland et al. [54]. The VF equation (Eq. 1) is simply a modified Arrhenius expression, which includes an increasing degree of interaction between random local relaxation processes, in this case of the dipolar response:

$$f = f_0 \cdot e^{-\frac{E_a}{k(T_m - T_{VF})}}, \tag{1}$$

where f is the frequency of the perturbation (applied ac field frequency, Hz); f_0 is the fundamental attempt or limiting response frequency of the dipoles (Hz); E_a is the activation energy of local polarisation (J); T_m is the temperature (K) of maximum dielectric permittivity at frequency f; T_{VF} is the characteristic VF temperature (often described as the static freezing temperature (K) [52, 53]); and k is Boltzmann constant (1.38×10^{-23} J K^{-1} or 8.617×10^{-5} eV K^{-1}).

By plotting the natural logarithm of applied frequency (f) against temperature of the dielectric permittivity maximum (T_m) [54], the following representation of data is obtained (Fig. 5). VF analysis often results in unreliable and unphysical values for the fitting parameters [64–67] primarily due to the sensitivity of fitting to the curvature of $T_m(f)$ data (usually obtained over a limited frequency range, e.g. 10–10^6 Hz) and the subsequent extrapolation which is often over several orders of magnitude; our experience has also found that sample quality is also critical, particularly for polycrystalline ceramics where microstructural factors such as grain size and sample density can have a dramatic effect on the values of T_m. From these VF curves shown in Fig. 5, it is apparent that
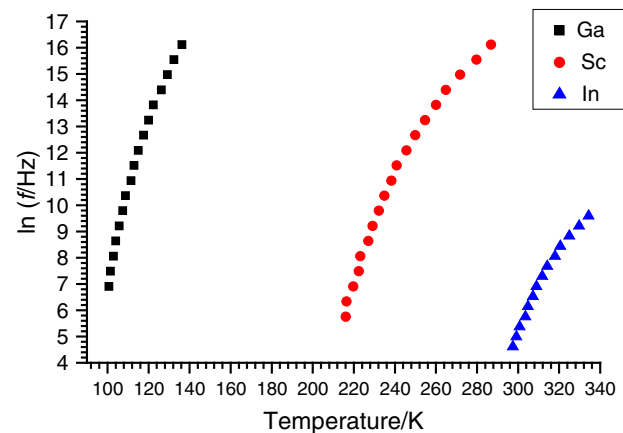

Fig. 5 Vogel–Fulcher curves for all three $Ba_6M^{3+}Nb_9O_{30}$ analogues (M = Ga, Sc, In)

with increasing ionic radius of the M species on the B-site, the degree of relaxor behaviour increases as denoted by the increased T_m range (curvature of plots); the obtained VF-like curves resemble the ones obtained previously [43], but in this case, due probably to different processing, additional features appeared in the dielectric permittivity, altering therefore the T_m values obtained. The dipole freezing temperatures may not simply increase linearly as a function of cation size, as suggested in our previous work [42]; the extrapolation of curves in Fig. 5 may result in dramatically different values than those observed in Ref. [42]. The Ga analogue displays the least relaxor behaviour as denoted by the smaller range of T_m values and the more linear and vertical VF curve (Fig. 5).

With increasing the M^{3+} radius, the VF curves are shifted to higher temperatures and the possibility of obtaining T_m values at low frequencies increases. This is because data at low frequencies are typically rather noisy, especially when approaching low temperatures. VF "free-fits" (where all three parameters: T_{VF}, f_0 and E_a are allowed to vary) of $T_m(f)$ extracted from dielectric permittivity data for Ga, Sc and In analogues are shown in Fig. 6; the VF parameters obtained are presented in Table 3. It is worth mentioning that T_{VF} is determined from the point at which the plotted curve goes vertical (i.e., ln $f \to -\infty$) and f_0 where the curve goes horizontal ($T_m \to \infty$).

For the In analogue, the E_a and, in particular, ln f_0 values seem to be small—it is almost within the experimentally measurable limit, while T_{VF} is ca. 30 K larger in comparison to that determined in Ref. [42]. It is worth noting, however, as we mentioned before, that due to limitations in the experimental set-up, it was not possible to record dielectric permittivity data above 340 K (Fig. 4); this restricts the range of T_m values available for the In sample at high frequencies (Fig. 5) and will therefore affect fitting and evaluation of the VF parameters. Although the VF
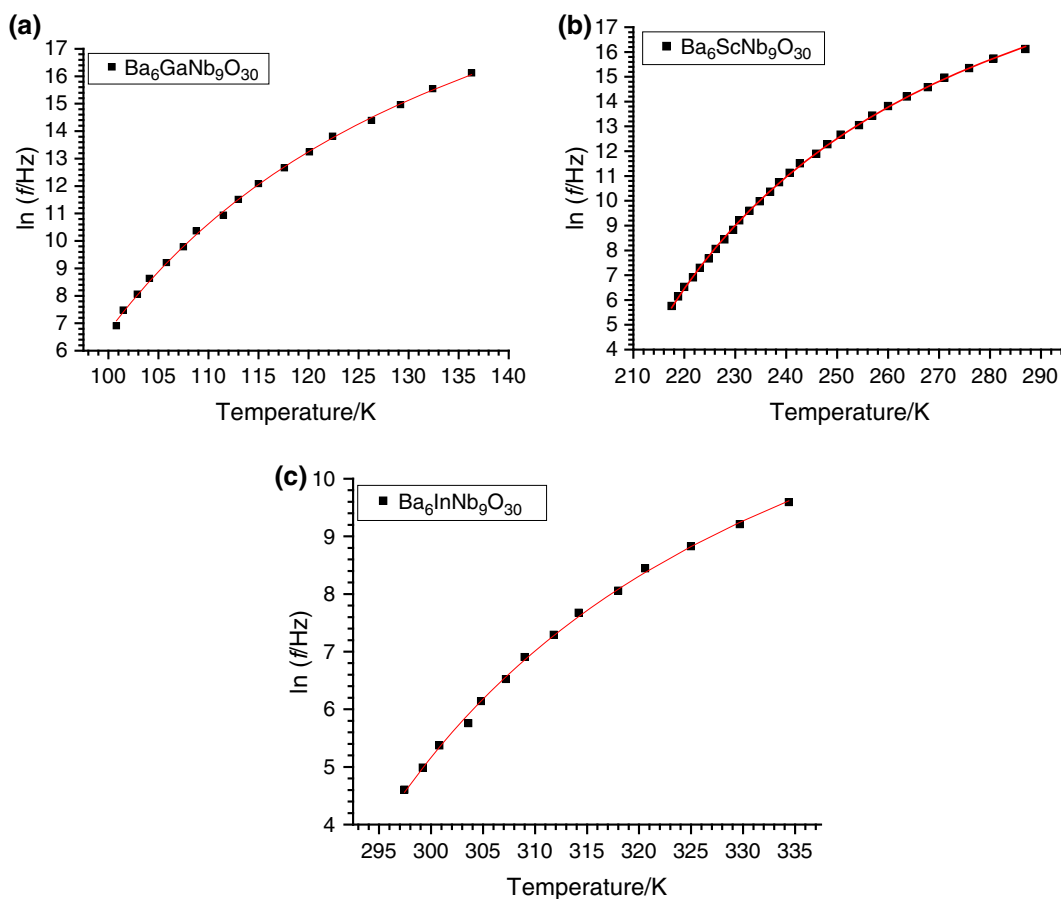
Fig. 6 Vogel–Fulcher "free-fits" of $T_m(f)$ from dielectric permittivity data for Ga (**a**), Sc (**b**) and In (**c**) analogues

Table 3 Vogel–Fulcher and goodness-of-fit parameters for $Ba_6M^{3+}Nb_9O_{30}$ (M^{3+} = Ga^{3+}, Sc^{3+}, In^{3+}) determined from fits shown in Fig. 6

Compound	T_{VF}/K	f_0/Hz	$\ln f_0$/Hz	E_a/eV	χ^2
$Ba_6GaNb_9O_{30}$	59.60 ± 2.48	3.13×10^{11} ± 2	26.47 ± 0.68	0.0688 ± 0.0064	0.08961
$Ba_6ScNb_9O_{30}$	154.07 ± 1.49	1.66×10^{11} ± 3	25.83 ± 0.26	0.1101 ± 0.0038	0.05558
$Ba_6InNb_9O_{30}$	253.06 ± 3.52	6.50×10^{6} ± 2	15.69 ± 0.54	0.0425 ± 0.0054	0.06277

free-fit looks reasonable for the In analogue (Fig. 6c), some physically sensible restriction on the fit parameters could provide more physically sensible results.

In Fig. 7 of Ref. [42], an upper limit for T_{VF} would be approximately 220 K; in this study, therefore, T_{VF} was set at the fixed value of 220 K. The data were also fitted with a lower limit for f_0 fixed at 2.26×10^{11} Hz which was determined from the average of that observed for the Ga and Sc analogues in Ref. [42]. The resulting restricted VF fits of the In analogue data with fixed T_{VF} and $\ln f_0$ parameters are presented in Fig. 7, with the results of the fit listed in Table 4.

Visual inspection of Fig. 7 shows that the restricted VF fits give a reasonable representation of the data but with

deviations at the extreme frequencies of the collected data. Figure 7b suggests that imposing a much too high value for f_0 would increase the activation energy in such way that the resulting T_{VF} value will be unrealistically low (Table 4). However, it is possible that any additional (parasitic) dielectric process may affect the true shape of the main process in the VF representation, and that the restricted fit, with fixed f_0 of 2.26×10^{11} Hz, may actually better describe the main relaxation process if the influence of the additional process is somehow deconvoluted and removed; this possibility will be studied in a subsequent paper.

Since for the free-fit of In analogue data, the T_{VF} value is higher than expected (253 K)—while the other two VF
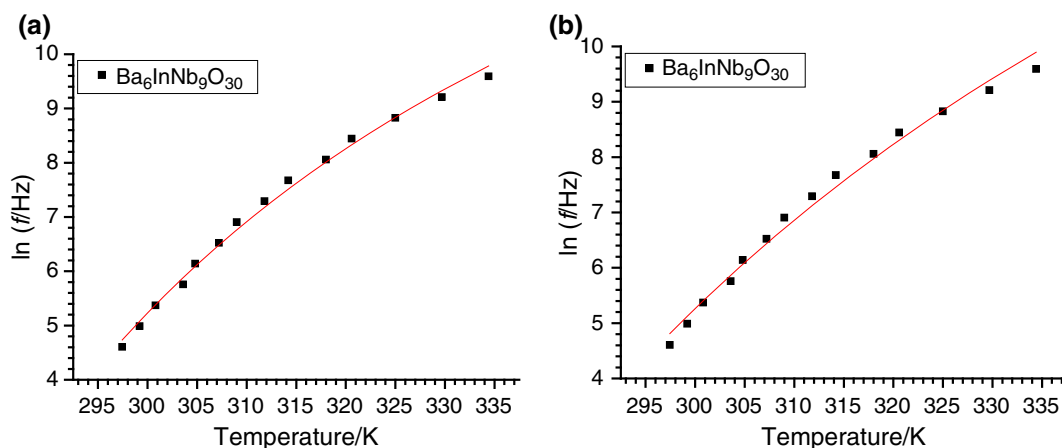
Fig. 7 Vogel–Fulcher restricted fits of $T_m(f)$ extracted from dielectric permittivity data for $Ba_6InNb_9O_{30}$; fixed $T_{VF} = 220$ K (**a**) and fixed $f_0 = 2.26 \times 10^{11}$ Hz (**b**)

Table 4 Vogel–Fulcher and goodness-of-fit parameters for $Ba_6InNb_9O_{30}$ data for the free-fit, imposed T_{VF} of 220 K and imposed average value of f_0 ($<\ln f_0> = 26.15$)

Compound	T_{VF}/K	f_0/Hz	$\ln f_0$/Hz	E_a/eV	χ^2
$Ba_6InNb_9O_{30}$	253.06 ± 3.52	$6.50 \times 10^6 \pm 2$	15.69 ± 0.54	0.0425 ± 0.0054	0.06277
$Ba_6InNb_9O_{30}$	220 imposed	$6.98 \times 10^8 \pm 1$	20.36 ± 0.27	0.1043 ± 0.0021	0.11910
$Ba_6InNb_9O_{30}$	179.27 ± 3.94	2.26×10^{11} imp.	26.15 imp.[a]	0.2173 ± 0.0066	0.17030

[a] imposed value $\ln f_0$ representing the average of the obtained values for Ga and Sc compounds in Ref. [42] ($<\ln f_0> = 26.15$)

parameters are too low ($f_0 = 6.50 \times 10^6$ Hz; $E_a = 0.0425$ eV), and on the other hand the imposed $f_0 = 2.26 \times 10^{11}$ Hz results in an unsatisfactory fit which provides a low value for T_{VF} (179.3 K), it becomes evident that according to the In data in Fig. 5, the fit has to flatten towards f_0 values that shall be either higher than 6.98×10^8 Hz but lower than 1.66×10^{11} Hz. Therefore, it raises the possibility for increasing the T_{VF} value from 180 to 220 K, of course the most probable case is somewhere in between, as shown in Fig. 8.

In order to investigate the influence on the fit parameters of the limited domain of frequencies where from the T_m values were obtained in the case of the In sample, the working domains for Ga and Sc analogues were restricted (Fig. 9a) to that obtained for the In analogue. The upper and lower limits are crucial as these regions display the most curvature, and it is therefore expected that these will have a large influence on the fit.

Restricting the frequency range for the Ga analogue to that of the In analogue, as shown in Fig. 9a, resulted in a near straight line and thus in the impossibility of performing a satisfactory VF fit—the parameters are not physically realistic. While for the Sc analogue, a free-fit over the selected low frequency range of T_m data provided a T_{VF} value which is 68 K smaller than that obtained for the free-
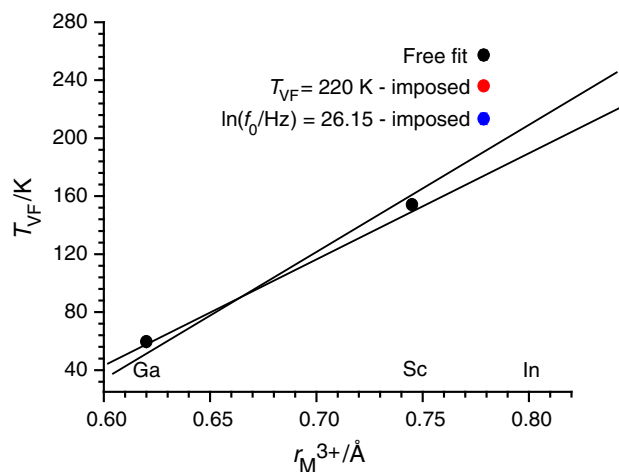

Fig. 8 Dependence of characteristic Vogel–Fulcher temperature, T_{VF}, on M^{3+} B-site cation radius. T_{VF} for the In analogue was determined (*i*) by a "free-fit", (*ii*) by fixed T_{VF} and (*iii*) by fixed f_0. The solid lines are lines of best fit for Ga, Sc and In data using (*ii*) and (*iii*)

fit over the entire range, and a f_0 value of 2.43×10^{18} Hz, which is too large to be physical (Table 5).

As reported previously [42, 43], even in the case of T_m data sets collected over a wider frequency range, it is
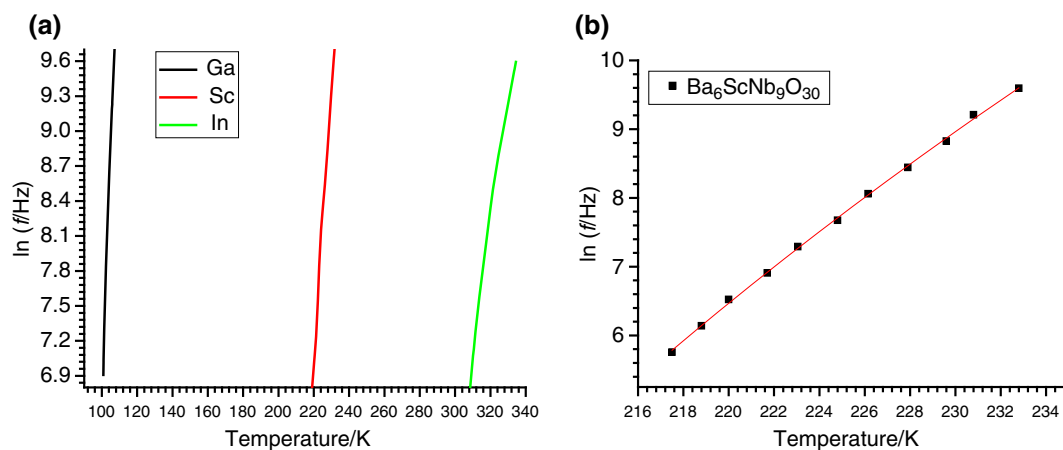
Fig. 9 Vogel–Fulcher representation of the dielectric permittivity data for all three $Ba_6M^{3+}Nb_9O_{30}$ analogues (M = Ga, Sc, In) over a limited frequency range (**a**) and Vogel–Fulcher restricted fit of Sc analogue in this limited frequency range (**b**)

Table 5 Vogel–Fulcher and goodness-of-fit parameters for $Ba_6ScNb_9O_{30}$ determined from free-fits of data over the entire and selected frequency ranges

Compound	T_{VF}/K	f_0/Hz	$\ln f_0$/Hz	E_a/eV	χ^2
$Ba_6ScNb_9O_{30}$*	154.1 ± 1.5	$1.66 \times 10^{11} \pm 3$	25.83 ± 0.26	0.1101 ± 0.0038	0.05558
$Ba_6ScNb_9O_{30}$**	86.2 ± 44.6	$2.43 \times 10^{18} \pm 7.5 \times 10^4$	42.34 ± 11.23	0.4136 ± 0.2680	0.03962

* Entire available frequency range

** In analogue limiting frequency range

extremely difficult to obtain reliable values for T_{VF}, f_0 and E_a from the VF fitting of such curves. It is obvious that when extrapolating from the most linear part of the curve (essentially the experimental points on the VF curve), this process is a very sensitive one, especially for the case of T_{VF} and f_0—with small differences in the experimental data inducing large variations in the parameters of the fit. Missing even one T_m value may induce large variations of the fit parameters.

Conclusions

In this paper, the in-depth analysis of the relaxor behaviour of $Ba_6MNb_9O_{30}$ (M = Ga, Sc, In) tetragonal tungsten bronze ceramics revealed that with the stepwise increase of the ionic radius of the M^{3+} cation on the B-site within the series, the VF curves $\ln f$ versus T_m are displaced to higher temperatures while the degree of relaxation increases. The extrapolation of the VF fit for different samples of Sc and In analogues prepared once more under similar synthesis conditions to those studied in Ref. [42] provided very different fit parameters than those obtained previously; the linear trend of the freezing temperature of dipoles, T_{VF}, with M^{3+} cation size within the series is no longer observed because

the dielectric data are very sensitive to preparative conditions and also because of uncertainties produced by the VF fitting itself. In particular, the magnitude of T_{VF} varied significantly within samples of the same composition.

Besides the regular "free-fits", by imposing fixed T_{VF} or f_0 parameters as extreme possibilities in the VF equation (representing physically sensible values obtained in Ref. [42]), reasonable or even very good representation and fitting of the data, and numeric results for the other fundamental relaxation parameters were obtained. It was shown that VF fits can provide inconsistent and random fundamental parameters for the dielectric relaxation processes with respect to the reproducibility and validity of the results. For further restricting the frequency domain—due to impossibility of data collection or due to imposed restrictions, missing even one T_m value may induce large variations of the fitting fundamental parameters.

Generally, conclusions could not be drawn only from fitting parameters obtained by the VF expression; as a more general recommendation, when reporting a set of relaxation parameter values, the careful understanding and selection of raw dielectric data is important, while the fit should not be carried out blindly only by using a simple "free-fit", but primarily by choosing and assuming a realistic imposed fit if required.

References

1. Shrout TR, Zhang SJ. Lead-free piezoelectric ceramics: alternatives for PZT? J Electroceramics. 2007;19:111–24.

2. Catalan G, Scott JF. Physics and applications of bismuth ferrite. Adv Mater. 2009;21:1–2463–1–2485.

3. Spaldin NA, Fiebig M. The renaissance of magnetoelectric multiferroics. Science. 2005;309:391–2.

4. Eerenstein W, Mathur ND, Scott JF. Multiferroic and magneto-electric materials. Nature. 2006;442:759–65.

5. Bokov AA, Ye Z-G. Recent progress in relaxor ferroelectrics with perovskite structure. J Mater Sci. 2006;41:31–52.

6. Smolenskii GA, Yudin VM, Sher ES, Stolypin YE. Antiferro-magnetic properties of some perovskite. Sov Phys JETP. 1963;16:622–4.

7. Sugawara F, Iida S, Syono Y, Akimoto S. Magnetic properties and crystal distortions of $BiMnO_3$ and $BiCrO_3$. J Phys Soc Jpn. 1968;25:1553–8.

8. Chiba H, Atou T, Syono Y. Magnetic and electrical properties of $Bi_{1-x}Sr_xMnO_3$: hole-doping effect on ferromagnetic perovskite $BiMnO_3$. J Solid State Chem. 1997;132:139–43.

9. Kimura T, Goto T, Shintani U, Ishizaka K, Arima T, Tokura T. Magnetic control of ferroelectric polarisation. Nature. 2003;426:55–8.

10. Lottermoser T, Lonkai T, Amann U, Hohlwein D, Ihringer J, Fiebig M. Magnetic phase control by an electric field. Nature. 2004;430:541–4.

11. Miller AJ (2010) Undergraduate research project. University of St Andrews.

12. Arnold DC, Morrison FD. B-cation effects in relaxor and ferroelectric tetragonal tungsten bronzes. J Mater Chem. 2009;19:6485–8.

13. Simon A, Ravez J. Solid-state chemistry and non-linear properties of tetragonal tungsten bronzes materials. C R Chim. 2006;9:1268–76.

14. Wang DH, Goh WC, Ning M, Ong CK. Effect of Ba doping on magnetic, ferroelectric, and magnetoelectric properties in mutiferroic $BiFeO_3$ at room temperature. Appl Phys Lett. 2006;88:212907.

15. Yuan GL, Or SW. Structural transformation and ferroelectro-magnetic behavior in single-phase $Bi_{1-x}Nd_xFeO_3$ multiferroic ceramics. Appl Phys Lett. 2006;88:062905.

16. Wang C, Takahashi M, Fujino M, Zhao X, Kume E, Horiuchi T, Sakai S. Leakage current of multiferroic $(Bi_{0.6}Tb_{0.3}La_{0.1})FeO_3$ thin films grown at various oxygen pressures by pulsed laser deposition and annealing effect. J Appl Phys. 2006;99:054104.

17. Chung C-F, Lin JP, Wu J-M. Influence of Mn and Nb dopants on electric properties of chemical-solution-deposited $BiFeO_3$ films. Appl Phys Lett. 2006;88:242909.

18. Kim JK, Kim SS, Kim W-J, Bhalla AS, Guo R. Enhanced ferroelectric properties of Cr-doped BiFeO3 thin films grown by chemical solution deposition. Appl Phys Lett. 2006;88:132901.

19. Stennett MC, Miles GC, Sharman J, Reaney IM, West AR. A new family of ferroelectric tetragonal tungsten bronze phases, $Ba_2MTi_2X_3O_{15}$. J Eur Ceram Soc. 2005;25:2471–5.

20. Stennett MC, Reaney IM, Miles GC, Woodward DI, West AR, Kirk CA, Levin I. Dielectric and structural studies of $Ba_2MTi_2Nb_3O_{15}$ ($BMTNO_{15}$, $M = Bi^{3+}$, La^{3+}, Nd^{3+}, Sm^{3+}, Gd^{3+}) tetragonal tungsten bronze-structured ceramics. J Appl Phys. 2007;101:104114.

21. Chen XM, Yang JS. Dielectric characteristics of ceramics in $BaO–Nd_2O_3–TiO_2–Ta_2O_5$ system. J Eur Ceram Soc. 1999;19:139–42.

22. Chen XM, Liu CL, Yang JS, Wu YJ. Some tungsten-bronze compounds in the $BaO–Nd_2O_3–TiO_2–Ta_2O_5$ system. J Solid State Chem. 1999;148:438–41.

23. Slater PR, Irvine JTS. Synthesis and electrical characterisation of the tetragonal tungsten bronze type phases, $(Ba/Sr/Ca/La)_{0.6}M_x$-$Nb_{1-x}O_{3-\delta}$ ($M = Mg$, Ni, Mn, Cr, Fe, In, Sn): evaluation as potential anode materials for solid oxide fuel cells. Solid State Ionics. 1999;124:61–72.

24. Van Uitert LG, Rubin JJ, Grodkiewicz WH, Bonner WA. Some characteristics of Ba, Sr, Na niobates. Mater Res Bull. 1969;4: 63–73.

25. Van Uitert LG, Levinstein NJ, Rubin JJ, Capio CD, Dearborn EF, Bonner WA. Some characteristics of niobates having "filled" tetragonal tungsten bronze-like structures. Mater Res Bull. 1968;3:47–57.

26. >Wemple SH, DiDomenico M, Camlibel I. Relationship between linear and quadratic electro-optic coefficients in $LiNbO_3$, $LiTaO_3$, and other oxygen-octahedra ferroelectrics based on direct measurement of spontaneous polarization. Appl Phys Lett. 1968;12: 209–11.

27. Jamieson PB, Abrahams SC, Bernstein JL. Ferroelectric tungsten bronze-type crystal structures. I. Barium strontium niobate $Ba0.27Sr0.75Nb2O5$. J Chem Phys. 1968;48:5048–57.

28. Jamieson PB, Abrahams SC, Bernstein JL. Ferroelectric tungsten bronze-type crystal structures. II. Barium sodium niobate $Ba(4 + x)Na(2-2x)Nb10O30$. J Chem Phys. 1969;50:4352–63.

29. Cheng TS, Amzallag E, Rokni M. Ferroelectricity measurements on $Sr_xBa_{1-x}Nb_2O_6$. Ferroelectrics. 1972;3:57–8.

30. Castel E, Josse M, Michau D, Maglione M. Flexible relaxor materials: $Ba_2Pr_xNd_{1-x}FeNb_4O_{15}$ tetragonal tungsten bronze solid solution. J Phys. 2009;21:452201.

31. Josse M, Bidault O, Roulland F, Castel E, Simon A, Michau D, Von der Muhll R, Nguyen O, Maglione M. The $Ba_2LnFeNb_4O_{15}$ "tetragonal tungsten bronze": towards RT composite multiferroics. Solid State Sci. 2009;11:1118–23.

32. Castel E, Josse M, Roulland F, Michau D, Raison L, Maglione M. In-situ formation of barium ferrite in iron-doped "tetragonal tungsten bronze": elaboration of room temperature multiferroic composites. J Magn Magn Mater. 2009;321:1773–7.

33. Albino M, Veber P, Pechev S, Labrugere C, Velazquez M, Maglione M, Josse M. Growth and characterization of $Ba_2LnFeNb_4O_{15}$ (Ln = Pr, Nd, Sm, Eu) relaxor single crystals. Cryst Growth Des. 2014;14:500–12.

34. Gardner J, Morrison FD. A-site size effect in a family of unfilled ferroelectric tetragonal tungsten bronzes: $Ba_4R_{0.67}Nb_{10}O_{30}$ (R = La, Nd, Sm, Gd, Dy and Y). Dalton Trans. 2014;43:11687–95.

35. Fang PH, Roth RS, Johnson H. Class of nonlinear dielectric materials. J Am Ceram Soc. 1960;43:169.

36. Foster MC, Brown GR, Nielson RM, Abrahams SC. $Ba_6CoNb_9O_{30}$ and $Ba_6FeNb_9O_{30}$: two new tungsten-bronze-type ferroelectrics. Centrosymmetry of $Ba_{5.2}K_{0.8}U_{2.4}Nb_{7.6}O_{30}$ at 300 K. J Appl Crystallogr. 1997;30:495–501.

37. Ismailzade I, Huseynov NG, Sultanov GJ, Hajiyev EM. Dielectric mossbauer and magnetic investigations of ferroelectric-magnetics $Sr_6Nb_9FeO_{30}$ and $Ba_6Nb_9FeO_{30}$. Ferroelectrics. 1976;13:389–91.

38. Liu PP, Wu SY, Zhu XL, Chen XM, Liu XQ. Structure, dielectric and magnetic properties of $Ba_6FeNb_9O_{30}$ tungsten bronze ceramics. J Mater Sci. 2011;22:866–71.

39. Damjanovic D. Ferroelectric, dielectric and piezoelectric properties of ferroelectric thin films and ceramics. Rep Prog Phys. 1998;61:1267.

40. Hirota K, Wakimoto S, Cox DE. Neutron and x-ray scattering studies of relaxors. J Phys Soc Jpn. 2006;75:111006.

41. Cross LE. Ferroelectric ceramics: tailoring properties for specific applications. In: Setter N, Colla EL, editors. Ferroelectric ceramics. Basel: Birkhauser; 1993.

42. Rotaru A, Arnold DC, Daoud-Aladine A, Morrison FD. Origin and stability of the dipolar response in a family of tetragonal tungsten bronze relaxors. Phys Rev B. 2011;83:184302.

43. Rotaru A, Miller AJ, Arnold DC, Morrison FD. Towards novel multiferroic and magnetoelectric materials: dipole stability in tetragonal tungsten bronzes. Philos Trans R Soc A. 2014;372:20120451.

44. Chi EO, Gandini A, Ok KM, Zhang L, Halasyamani PS. Syntheses, structures, second-harmonic generating, and ferroelectric properties of tungsten bronzes: A6M2 M'8O30 ($A = Sr2 +$, Ba2 +, or Pb2 +; $M = Ti4 +$, Zr4 +, or Hf4 +; M'= Nb5 + or Ta5 +). Chem Mater. 2004;16:3616–22.

45. Neurgaonkar RR, Nelson JG, Oliver JR. Ferroelectric properties of the tungsten bronze $M_6^{2+}M_2^{4+}Nb_8O_{30}$ solid solution systems. Mater Res Bull. 1992;27:677–84.

46. Young SE, Guo HZ, Ma C, Kessler MR, Tan X. Thermal analysis of phase transitions in perovskite electroceramics. J Therm Anal Calorim. 2014;115:587–93.

47. de la Rubia MA, Alonso RE, de Frutos J, Lopez-Garcia AR. Phase transitions in $PbTi_xHf_{1-x}O_3$ determined by thermal analysis and impedance spectroscopy. J Therm Anal Calorim. 2009;98:793–9.

48. Runt JP, Fitzgerald JJ. Dielectric spectroscopy of polymeric materials. New York: American Chemical Society; 1997.

49. Leonardi A, Dantras E, Dandurand J, Lacabanne C. Dielectric relaxations in PEEK by combined dynamic dielectric spectroscopy and thermally stimulated current. J Therm Anal Calorim. 2013;111:807–14.

50. Craig DQM. Applications of low frequency dielectric spectroscopy to the pharmaceutical sciences. Drug Develop Ind Pharm. 1992;18:1207–23.

51. Johari GP, Kim S, Shanker RM. Dielectric relaxation and crystallization of ultraviscous melt and glassy states of aspirin, ibuprofen, progesterone, and quinidine. J Pharm Sci. 2007;96:1159–75.

52. Vogel H. Das temperaturabhängigkeitsgesetz der viskosität von flüssigkeiten. Phys Z. 1921;22:645–6.

53. Fulcher GS. Analysis of recent measurements of the viscosity of glasses. J Am Ceram Soc. 1925;8:339–55.

54. Viehland D, Jang SJ, Cross LE, Wuttig M. Freezing of the polarization fluctuations in lead magnesium niobate relaxors. J Appl Phys. 1990;68:2916–21.

55. Saslow WM. Scenario for the Vogel-Fulcher"law". Phys Rev B. 1988;37:676.

56. Rietveld HM. A profile refinement method for nuclear and magnetic structures. J Appl Cryst. 1969;2:65–71.

57. von Dreele RB, Larson AC. General structure analysis system (GSAS). California: University of California; 2001.

58. Shannon RD. Revised effective ionic radii and systematic studies of interatomic distances in halides and chalcogenides. Acta Crystallogr. 1976;A32:751–67.

59. Newnham RE. Structure-property relations in ceramic capacitors. J Mater Educ. 1983;5:947–82.

60. Fu D, Taniguchi H, Itoh M, Koshihara S, Yamamoto N, Mori S. Relaxor $Pb(Mg_{1/3}Nb_{2/3})O_3$: a ferroelectric with multiple inhomogeneities. Phys Rew Lett. 2009;103:207601.

61. Badapanda T, Rout SK, Cavalcante LS, Sczancoski JC, Panigrahi S, Sinha TP, Longo E. Structural and dielectric relaxor properties of yttrium-doped $Ba(Zr_{0.25}Ti_{0.75})O_3$ ceramics. Mater Chem Phys. 2010;121:147–53.

62. Cross LE, Jang SJ, Newnham RE, Nomira S, Uchino K. Large electrostrictive effects in relaxor ferroelectrics. Ferroelectrics. 1980;23:187–91.

63. Kerfah A, Taibi K, Guehria-Laidoudi A, Simon A, Ravez J. $Ba_{1-x}A_x(Ti_{0.7}Zr_{0.3})O_3$ and $(Ti_{0.7}Zr_{0.3})O_3$ compositions ($A = Ca$, Sr; $A' = Y$, La, Bi). Solid State Sci. 2006;8:613–8.

64. Zhu XL, Chen XM. Thermal hysteresis of ferroelectric transition in $Sr_4R_2Ti_4Nb_6O_{30}$ ($R = Sm$ and Eu) tetragonal tungsten bronzes. Appl Phys Lett. 2010;96:032901.

65. Du H, Zhou W, Luo F, Zhu D, Qu S, Pei Z. Perovskite lithium and bismuth modified potassium-sodium niobium lead-free ceramics for high temperature applications. Appl Phys Lett. 2007;91:182909.

66. Bahri F, Khemakhem H, Gargouri M, Simon A, Von der Muhll R, Ravez J. Dielectric and Raman studies on the solid solution $(1 - x)$ $BaTiO_3/xNaNbO_3$ ceramics. Solid State Sci. 2003;5:1445–50.

67. Du H, Zhou WC, Luo F, Zhu F, Qu D, Pei Z. Phase structure, dielectric properties, and relaxor behavior of $(K_{0.5} Na_{0.5})NbO_3$–$(Ba_{0.5}Sr_{0.5})TiO_3$ lead-free solid solution for high temperature applications. J Appl Phys. 2009;105:124104.